Experiments in Fluids (2023) 64:150
https://doi.org/10.1007/s00348-023-03691-y

RESEARCH ARTICLE

Experimental study on internal flow structure and dynamics of dense liquid-particle flow down inclined channel

Yunhui Sun[1] · Jiajun Jiao[1] · Yi An[2] · Xiaoliang Wang[1] · Qingquan Liu[1]

Received: 13 March 2023 / Revised: 5 June 2023 / Accepted: 30 July 2023 / Published online: 20 August 2023
© The Author(s), under exclusive licence to Springer-Verlag GmbH Germany, part of Springer Nature 2023

Abstract

Dense granular flows widely exist in the environment and industry where inter-particle interactions play essential role. Studying the flow behaviour is important for a better understanding and more scientific description of the granular rheology. This paper experimentally investigates liquid-particle mixture dense flows down an inclined channel with bumpy-frictional base. The refractive index matching method is used which permits the determination of the internal flow information, including the velocity, shear rate, granular temperature and solid concentration. It is observed that the wall influence is minor at the observing position. The pressure and shear stress obtained from the integration of the solid concentration matches well with the prediction of the kinetic theory. The particle interaction pattern is analysed from the rheology properties and a coherence length approach. The flow is found to be rheologically stratified, with the near-bottom being collision-dominated and the near-surface being friction-dominated. The bottom pore pressure and stress are also directly measured and analysed in combination with the internal kinetic properties.

1 Introduction

Liquid-particle mixture flows are commonly seen in natural flows such as debris flows, submarine avalanches, bedload transport and also industrial applications such as mining and food processing (Andreotti et al. 2013). Studying granular flow behaviour has essential practical importance and scientific meaning. This paper focuses on the typical granular flow condition of the liquid-particle mixture flow down an inclined channel. This flow is directly related to certain geological hazards such as landslides and debris flows, where a significant volume of materials flows downstream, risking human life and property. Because of the relatively small-scale, simple and well-controlled flow condition of the flow down an inclined channel, the stress can be balanced by gravity and easily obtained if the flow achieves a (near) steady state (Pouliquen 1999). This permits the flow to be seen as a rheometer to study the rheological behaviour of granular materials (MiDi 2004; Forterre and Pouliquen 2008) or suspensions (Bonnoit et al. 2010; Guazzelli and Pouliquen 2018).

The dry granular flow down an inclined channel has been widely studied and a variety of phenomena have been reported (Pouliquen 1999; Forterre and Pouliquen 2001; Silbert et al. 2001; Jop et al. 2005, 2006; Brodu et al. 2015; Meninno et al. 2018; Zhu et al. 2020). However, liquid-particle mixture flows differ from their dry counterparts because the liquid induces complex liquid-particle interactions and significantly changes the flow behaviour. Takahashi (1978) is believed to be the first to have used a flume test to study water-sediment mixture flows (debris flow). It was found that the debris flow propagates in three successive stages: a steep front, uniform central body and tail. Later works by Iverson et al. performed large-scale experiments by releasing saturated materials down a 95 m long, 2 m wide flume and studied the influence of basal boundary conditions and debris compositions (Iverson 1997; Iverson et al. 2010). Another distinctive flow scenario was by Lanzoni et al., who placed a layer of sediment in a 10 m long flume and triggered a debris flow by continuously releasing a controlled water discharge from an upstream water tank. They obtained a 2–5 s quasi-uniform flow of the central body and studied

✉ Xiaoliang Wang
wangxiaoliang52086@126.com

✉ Qingquan Liu
liuqq@bit.edu.cn

[1] School of Aerospace Engineering, Beijing Institute of Technology, Beijing 100081, China

[2] Key Laboratory for Mechanics in Fluid Solid Coupling Systems, Institute of Mechanics, Chinese Academy of Sciences, Beijing 100190, China

the velocity profiles and bulk concentration (Lanzoni 1993; Lanzoni et al. 2017). The aforementioned studies generally paid attention to the bulk properties such as the flow height, velocity and bulk concentration et al., while the simultaneous measurement of the local information such as the local velocity, solid concentration and more importantly the granular temperature (velocity fluctuation) have been less reported (Chauchat 2018).

Armanini et al. made a further step forward in investigating liquid-particle mixture flows. A recirculating system was used to achieve a long-period steady, uniform flow. Different flow regimes were observed depending on the channel inclination, including loose bed (immature, mature, plug flow) and solid bed regimes (Armanini et al. 2005; Larcher et al. 2007). Layer-averaged velocity, solid concentration, shear rate and granular temperature profiles along the depth were studied based on Voronoï methods (Capart et al. 2002; Spinewine et al. 2003). They found that the rheological behaviour is self-organised into sublayers where particle interactions are dominated by collision or friction from the relationship between the stress and shear rate. The results were further explained that the two behaviours coexist and exhibit intermittency switching between each other. An intermittency function was introduced to build a relationship between external and collision stresses based on kinetic theory (Armanini et al. 2009). Similar experiments were also reported by Capart and Fraccarollo (2011) to study the transport layer structure in sheet flows and were latter employed to study the fluid turbulent mixing length in liquid-particle mixture flows based on the kinetic energy and stress balance (Berzi and Fraccarollo 2015).

Despite the considerable progress made by the traditional experimental investigations, most of them could only observe the surface or near-wall flow properties given the non-transparent nature of the liquid-particle mixtures. The wall influence may result in a distorted flow and high three-dimensionality even in dry granular flows (Jop et al. 2005; Meninno et al. 2018), where the wall-particle friction retards the particle movement which is responsible for the steady flow at higher inclinations (Gollin et al. 2017). In liquid-particle mixture flows, the near-wall granular motion may be further retarded due to the fluid drag force, as evidenced in the studies by Armanini et al. (2005) and Rousseau and Ancey (2020). Besides, the wall serves as a solid elastic boundary to the flow which may alter the flow properties near wall. For example, based on stereoscopic imaging techniques, Matoušek et al. (2019) reported a higher fluctuation for the normal-to-wall velocity which is considered to be a result of wall-particle impact. Hanes and Walton (2000) found the reverse distribution of the granular temperature for the near-wall and near-center flows when studying the dry granular flow over a bumpy base. Therefore, it is considered that the internal flow information away from the wall is more representative of a true granular flow behaviour, which is almost immune of the sidewall effects and corresponds to an outcome of purely inter-particles and liquid-particles interactions. The refractive index matching (RIM) method provides a novel and helpful tool under such conditions (Dijksman et al. 2012; Wright et al. 2017). The mixture is made transparent by matching the refractive indexes of the liquid and particles, and the internal flow can be visualised using plane laser-induced fluorescence (PLIF) technique.

The RIM method was used in the study of debris flow by Sanvitale and Bowman (2012) and later by Sanvitale and Bowman (2016), who used graded particles. They obtained velocity and granular temperature results based on particle image velocimetry (PIV) and investigated the influence of particle size distributions and PIV patch size on granular temperature estimation. Ni and Capart (2015) developed a new recirculating system and applied the RIM scanning technique to simultaneously capture particle and liquid with particle tracking velocimetry (PTV). Detailed internal concentration, velocity and velocity fluctuation profiles of both the particles and the liquid were provided (Ni and Capart 2018). They analysed the vertical balance of stress and drag force based on the two-phase description of the liquid-particle mixture flow.

For dense granular flow, inter-particle interactions such as friction and collision are known to dominate the flow behaviour or rheology over other hydrodynamic forces (Guazzelli and Pouliquen 2018). Therefore, the inter-particle interactions may provide a more intrinsic description of the granular flow behaviour and the constitutive relation for the granular stress. However, these studies have not investigated the particle interaction pattern and its influence on the stress. Most studies focus on the granular flow over a loose bed which serve as an erodible bed while the flow over a bumpy solid bed which serves as a fluctuation energy injection source has been paid less attention especially for liquid-particle flows. Moreover, traditional experiments mainly focused on kinematic properties such as concentration, velocity, shear rate and fluctuation, while the stress is calculated based on gravity balance assumption which lacks experimental evidence. Direct measurement of the stress or pore pressure under the granular flow is possible (Iverson 1997; Iverson and George 2019; Roche et al. 2021), but their linkage with internal flow information has been less studied.

This paper is devoted to comprehensive measurement of the dense liquid-particle mixture flows down an inclined channel with bumpy-frictional base. The internal flow structure is obtained using the RIM method and PTV analysis. Direct measurements of the dynamic properties involving the bottom pore pressure and stress are performed to provide a more detailed and convincing picture of the flow. This is accomplished by developing new channel-flow equipment that integrates the RIM observations and simultaneous dynamics measurements. The remainder of this paper is organised as follows. Section 2 introduces the material properties and experimental equipment including the measuring system. Section 3 gives the PTV technique and the corresponding statistical method to obtain the internal flow information. The flow properties are described in Sect. 4 including the flow height, internal flow structure and their combined analysis with the direct sensor-measured stress. Section 5 concentrates on the relationship of the flow properties based on kinetic theory and analyses the particle interaction patterns. Section 6 summarises this paper and draws the conclusions.

2 Experimental setup and measuring system

2.1 Channel and materials

The experiments are performed in an 4 m long inclined channel with a rectangular cross-section having a width W = 200 mm and a height of 300 mm as shown in Fig. 1. The inclined angle of the channel θ is adjustable in the range of 0–16°. A 0.6 m high silo storing the liquid-particle mixture with a capacity of about 0.17 m^3 is located at the entrance of the channel to feed the flowing materials. The inner corner is fixed with an inclined plane to allow the materials to fully flow without forming a dead zone.

The silo is connected to the channel with a two-gate structure. A pneumatic butterfly valve makes the inner gate which regulates the release of the materials and can be fully opened within 0.5 s. The materials flow about 200 mm in a rectangular duct of width W before reaching the a steel plate (outer gate) which leaves a 40 mm opening above the channel base to reshape the flow into the channel's rectangular cross-section. Although this height can be modified by changing the gate opening height h_g, it is fixed at 40 mm in this study. The channel base is roughened with glued particles that are the same as the flowing particles. The flowing mixtures run out freely at the end of the channel and are collected in a tank.

The RIM method and the PLIF technique (Wiederseiner et al. 2010; Dijksman et al. 2012; Wright et al. 2017) are used to visualise the internal flow. The RIM has become a popular experimental tool in the investigations of granular

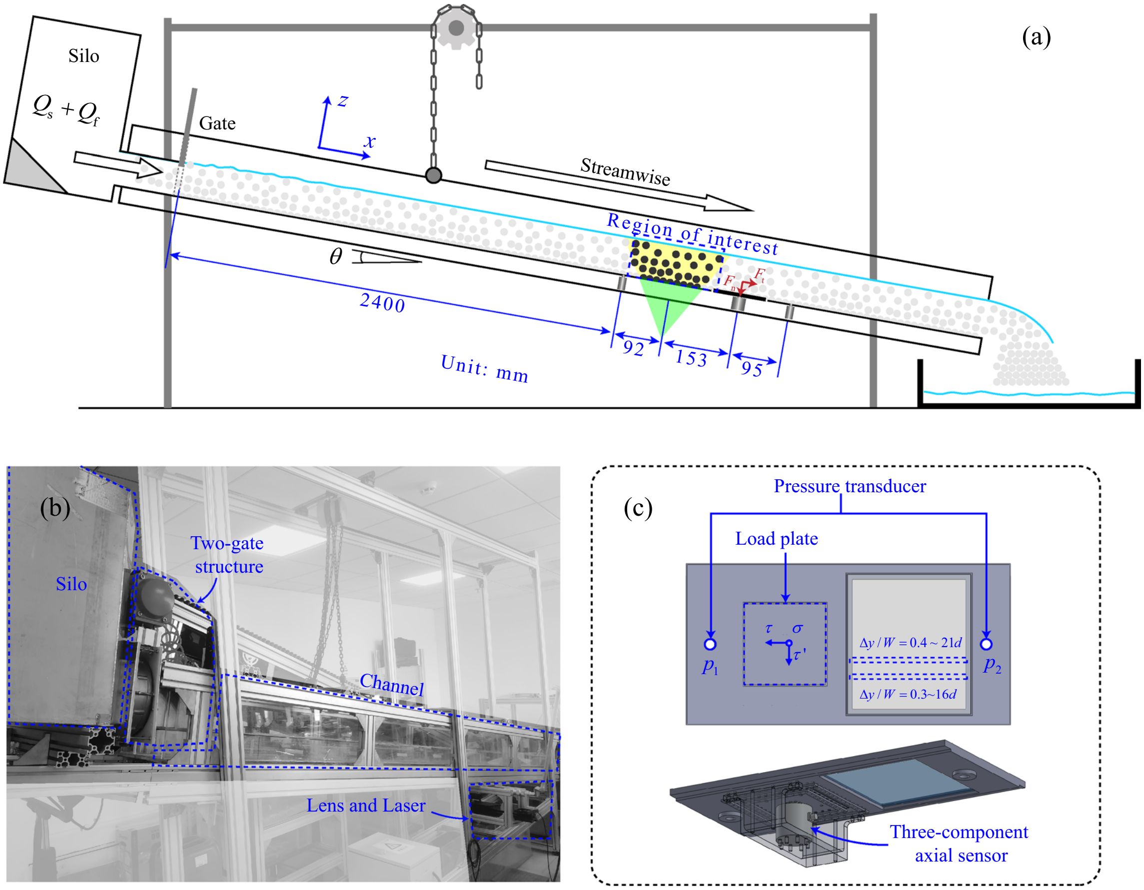

Fig. 1 **a** Schematic diagram and **b** photograph of the experiment setup. **c** The designed measuring plate with integrated sensors and the laser entrance glass plate. Two laser entrance positions are shown

materials in recent years (Houssais et al. 2015; Ferdowsi et al. 2017; Trewhela and Ancey 2021), which is a relatively simple and inexpensive tomographic technique to observe the inner information of the media. The basic idea is to match the refractive indexes of the specially selected transparent solid and liquid so that a transparent mixture is obtained. The liquid is premixed with fluorescent dye. A laser sheet is introduced to the mixture so that the particles and liquid are illuminated by the original laser and excited fluorescence, respectively. By using a longpass filter, the internal particles are visualized as dark circles and the liquid as brighter background.

Borosilicate glass beads with density $\rho_s = 2178$ kg × m^{-3} are used. The particle size distribution, which well follows a log-normal distribution, is given in Fig. 2 with an averaged diameter $d = 3.79$ mm. Note that the particles are nearly monodisperse with a small size variation range of about ±0.3 mm (≈ 8%), so the granular segregation is not likely to play a significant role. The particle-particle coefficient of restitution is $e = 0.91$ and coefficient of friction is $\mu_s = 0.47$, which is measured from a drop-bounce test and the repose angle, respectively, under the dry condition (Sun et al. 2020). The particles are closely refractive-index-matched with the dimethyl sulfoxide (DMSO) aqueous solution with a density of $\rho_f = 1095$ kg × m^{-3} and dynamic viscosity of $\mu_f = 2.37$ mPa × s. Moderate fluorescent dye Rhodamine 6 G is added to the liquid to enhance the contrast between the particles and liquid when imaged. Additional details of the visualisation technique are also referred to Sun et al. (2021), where this RIM system was used to study the immersed granular collapse problem. The particles and liquid are added into the silo layer by layer and carefully mixed to avoid trapped air bubbles. The initial granular packings in the silo are prepared in the same way for different groups, though the material volume V_0 may slightly vary as given in Table 1. The initial solid volume fraction is about 0.64 which is very close to a random close packing.

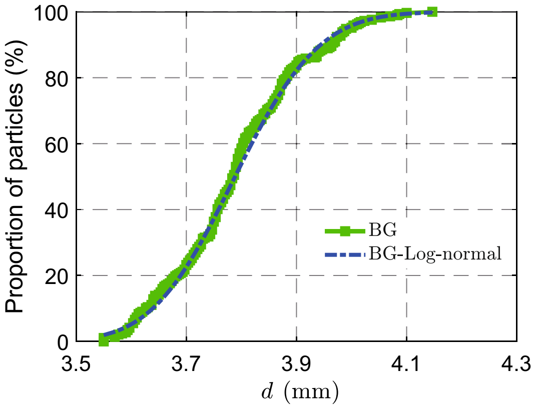

Fig. 2 Particles size distribution counting by number. The dash-dotted line is the corresponding log-normal fitting

2.2 Measuring system

The flow is measured at the position approximately 2.4 m from the channel inlet, where the flow is believed to be fully developed (see Appendix A) and to have achieved a quasi-steady state. A green laser beam (527 nm) from a 10 W power pulse laser generator (Vlite-Hi-10K, Beamtech Optronics Co., Ltd.) is transmitted by an articulated optical waveguide to a lens system fixed beneath the channel. A Powell lens expands the laser beam to a sheet aligned parallel to the streamwise direction of the channel. The laser waist position is adjusted to 40 mm above the channel base, aiming to reduce the effect of laser thickening due to scattering resulting from a slight mismatch between liquid and particle refractive indexes (Sanvitale and Bowman 2012). The laser sheet is 1−1.5 mm thick across the region of interest.

A high-speed camera (Fastcam MiniWX100, Photron) operates at a frame rate of 1000 frames per second and a resolution of 1532×464 pixels which corresponds to 193× 58 mm (≈0.126 mm per pixel) for at least 11 s to capture the internal flow images. A long wave pass filter (> 550 nm, OD4) enables the camera to discard the source laser and capture mainly the fluorescence to enhance the image contrast.

In addition to the imaging system, the bottom pore pressure and stress are also measured directly with sensors. The sensors are integrated into a specially designed basal plate, as shown in Fig. 1c. Two high-frequency-response, differential-pressure transducers (0–5 kPa, Precision: 25 Pa) are mounted at both ends of the plate and are covered with 3 mm gridded stainless steel meshes to protect the sensing unit. A triaxial piezoelectric sensor (0–20 N, Precision: 0.04 N) is fixed to the plate by a supporting structure. A 100× 100 mm load plate connected to the sensor is installed flush to the bed surface so that the sensor measures the normal F_n and shear forces F_t applied by the granular flow to the load plate. The normal stress is calculated by $\sigma = F_n/A$ and the shear stress by $\tau = F_t/A$, where A is the load plate area. An approximately 1 mm gap is left between the load plate edges and the surrounding basal plate to prevent the particles from dropping or jamming the gap and ensure that the plate can be freely loaded. Under the gap, a 0.1 mm thick silica membrane layer is applied to prevent liquid leaking and is sufficiently thin and soft to prevent any initial load from the membrane on the sensor. Note that all the sensors and the load plate are mounted along the channel's centreline. A borosilicate glass plate is placed between the triaxial piezoelectric sensor and the upstream pore pressure sensor where the laser sheet enters as shown in Fig. 1c.

The load plate was tested by burying it in a known weight of particles or by placing a known weight object at its centre.

By comparing, respectively, the measured value F_n and F_t with the normal component $W\cos\theta$ and tangential component $W\sin\theta$ of the total weight W applied on the load plate, it was found that the measured forces, especially the shear force, suffer from a bending effect when the force do not act through the center of the sensor especially when an inclination exists and induce a torque to the sensing unit. The bias may be as much as 10% for the shear force and 2% for the normal force, so the normal force is believed to be more reliable.

It is seen that the designed basal plate is integrated with the most in-channel units needed for the flow measurement, including the sensors and laser entrance plate. The basal measuring plate is also roughened with glued particles, but the laser entrance position is left unchanged for a gap of about $1.5d$ width to avoid the laser sheet distortion because the refractive index of the glue is not matched with the mixture. Two laser entrance positions $\Delta y/W$ of 0.3 and 0.4 are used in this paper, where Δy is the distance of the laser from the front sidewall (note that $\Delta y/W = 0.5$ when the laser enters directly from the channel's centreline). So the inner flow conditions are observed and it will be shown in Sect. 4 that the sidewall influence is almost negligible.

The experiments start by opening the pneumatic valve, and the camera is triggered manually within 1 s when the granular flow arrives the measuring plate. The camera outputs a positive-voltage signal upon triggering which is recorded with a data acquisition logger (LGR-5329, Measurement Computing Co.) together with the sensors' signal at a sampling rate of 10,000 Hz, which achieves the time synchronisation of the measuring system.

3 Analysis method

3.1 Image processing and statistical methods

The original experimental images are first equalised to correct longitudinal brightness variations following the procedure by Ni and Capart (2015) and adopting the background correction process proposed by Houssais et al. (2015). The particles are recognised using a circle detection method based on the phase-coding Circle Hough Transform (Atherton and Kerbyson 1999; Yuen et al. 1990) and are tracked using nearest-neighbour matching methods, given that the particle displacement is less than one particle radius per frame. The particle positions, radii and velocities are obtained from this procedure (Zhang et al. 2020; Sun et al. 2020, 2021). The uncertainty of the circle detection method has been examined to be less than one pixel when detecting a circle with radius of 16 pixels under normal noise level (Atherton and Kerbyson 1999), which corresponds to about 0.126 mm in the present experiment. Therefore, considering the frame rate, the particle velocity measurement uncertainty is generally less than 0.126 m/s. Assuming that the flow is steady, uniform and unidirectional, the measured area is divided into horizontal bins and the velocities are layer-averaged. The bin thickness is fixed at one particle diameter d which corresponds to approximately 32 pixels. In a specific statistical period t_s, for N_k particles located in the k^th bin with streamwise velocities $u_{i,k}$ and normal velocities $w_{i,k}$, the average velocities are given by

$$\bar{u}_k = \frac{\sum_{i=1}^{N_k} u_{i,k}}{N_k}, \quad \bar{w}_k = \frac{\sum_{i=1}^{N_k} w_{i,k}}{N_k}. \tag{1}$$

The fluctuation of particle velocity is defined as its deviation from the average as $u'_{i,k} = u_{i,k} - \bar{u}_k$ where $\bar{u}_k$ is linearly interpolated to the instantaneous local position in order to avoid spurious contributions to the fluctuations (Larcher et al. 2007). The outliers of the preliminary velocities satisfying $|u'_{i,k}| > 2\sqrt{\overline{u'^2_k}}$ are excluded, where $\sqrt{\overline{u'^2_k}}$ is the root-mean-squared (RMS) velocity fluctuations of the k^th bin. The filtered velocities are used for the analysis in the following. The granular temperature is calculated as $T_k = (\overline{u'^2_k} + \overline{w'^2_k})/2$. The fluctuations are calculated based on the Lagrangian velocity auto-correlations function (ACF) (Armanini et al. 2005; Perng et al. 2005) which is believed to be less affected by the measurement noise (see Appendix B).

Another significant value is the particle concentration or the solid volume fraction ϕ. From the Delesse principle, the area ratio of solid to the total area of an idealised thin plane cutting randomly packed particles is equal to ϕ in a statistical sense (Underwood 1969). Area of each detected particle is distributed to the corresponding bins based on their relative positions and the area ratio is calculated as the particle area divided by the bin area. The area ratio is averaged over period t_s (same as that for the velocity) to obtain the solid volume fraction ϕ.

This paper adopts $t_\mathrm{s} = 0.1$ s (corresponding to 100 frames) during which the flow properties are believed to remain steady, and the dataset is large enough to obtain meaningful statistical results. As will be examined in Sect. 4.1, the flow variation within $t_\mathrm{s} = 0.1$ s is negligible.

3.2 Stress calculations

By assuming that the liquid and particles are individually incompressible and no mass change occurs in between, the momentum equation of the liquid-granular mixture is given by (Iverson 1997)

$$\rho(\partial \boldsymbol{v}/\partial t + \boldsymbol{v}\cdot\nabla\boldsymbol{v}) = \nabla\cdot(\boldsymbol{T}_\mathrm{s} + \boldsymbol{T}_\mathrm{f} + \boldsymbol{T}') + \rho\boldsymbol{g}. \tag{2}$$

In this equation, $\rho = \phi\rho_\mathrm{s} + (1-\phi)\rho_\mathrm{f}$ and $\boldsymbol{v} = [\phi\rho_\mathrm{s}\boldsymbol{v}_\mathrm{s} + (1-\phi)\rho_\mathrm{f}\boldsymbol{v}_\mathrm{f}]/\rho$ are the mixture density and velocity, respectively, where $\boldsymbol{v}_\mathrm{s}$ and $\boldsymbol{v}_\mathrm{f}$ are the solid and fluid velocity vectors. $\boldsymbol{T}_\mathrm{s}$ and $\boldsymbol{T}_\mathrm{f}$ are the solid and fluid stress tensors, respectively, $\boldsymbol{T}'$ is the stress resulting from the relative motion of the solid or fluid to the mixture and $\boldsymbol{g}$ is the gravitational acceleration. For the two-phase dense granular flow investigated in this paper, we assume that the solid and fluid velocities $\boldsymbol{v}_\mathrm{s}$ and $\boldsymbol{v}_\mathrm{f}$ are equal, which is reasonable because the interstitial fluid is mainly carried by the particles. This assumption has been examined in our preliminary test (not shown here) by adding tracer particles to the fluid and has also been demonstrated in previous similar experiments (Cassar et al. 2005; Aussillous et al. 2013; Lanzoni et al. 2017). Therefore, the particle velocity is treated as the mixture velocity and $\boldsymbol{T}'$ can be neglected.

Traditionally, the left hand of Eq. (2) is neglected for steady, uniform granular flow, and a gravity-balanced stress distribution is obtained (Armanini et al. 2005; Houssais et al. 2016; Lanzoni et al. 2017; Maurin et al. 2018; Ni and Capart 2018). The shear and normal stresses are given by

$$\tau(z) = (T_\mathrm{s} + T_\mathrm{f})_{zx} = g \sin\theta \int_z^H \rho \mathrm{d}\xi + p_0 \sin\theta, \tag{3}$$

$$\sigma(z) = -(T_\mathrm{s} + T_\mathrm{f})_{zz} = g \cos\theta \int_z^H \rho \mathrm{d}\xi + p_0 \cos\theta, \tag{4}$$

where H is the flow height, to be determined in Sect. 4.1. The x-axis is along the streamwise direction and the z-axis is normal to the bottom plate whose zero point is taken at the surface of the flat plate, i.e. the glued particles are also included. The term p_0 represents the contribution of the near-surface particles to the stresses, meaning that the stress tends to a finite value when approaching the surface where nonzero shear rate and granular temperature exist (Armanini et al. 2009; Houssais et al. 2016). Here $p_0 = 0.5\rho_\mathrm{s} V_\mathrm{p}/A_\mathrm{p} = \rho_\mathrm{s} g d/3$, where V_p and A_p are the particle's volume and middle section area, respectively. This term's contribution is small deep in the flow but may be important near the surface. The fluid contribution to the shear force is negligible because both the viscous shear and the turbulence shear are believed much smaller than the inter-particle stress in dense granular flow considering the high packing density ($\phi \gtrapprox 0.3$) (Berzi and Fraccarollo 2015; Maurin et al. 2016). So the shear force given by Eq. (3) is seen as the effective inter-particle shear force.

Furthermore, we assume that the buoyancy-reduced weight of the particle is entirely supported by the inter-particle contact, i.e. the hydrodynamic contribution is negligible. The granular pressure or the effective normal stress can be expressed as

$$\sigma'(z) = (\rho_\mathrm{s} - \rho_\mathrm{f}) g \cos\theta \int_z^H \phi \mathrm{d}\xi + p_0 \cos\theta. \tag{5}$$

Note that this expression actually treats the fluid pressure as hydrostatic, which is examined in Sect. 4.3.

4 Results

4.1 Overview of the flow process

In the experiments, it was observed that the heights of particles and liquid are close. Only a small portion of the particles emerged from the liquid, with a height of less than $d/2$. The flow height is determined based on the transverse average of the image brightness, $I(z_j) = \sum_{i=1}^{N} I(x_i, z_j)$ where $I(x_i, z_j)$ is the brightness of the pixel at (x_i, z_j) and N is the image's transverse length. As shown in Fig. 3, $I(z_j)$ oscillates near the flow surface. A high value is first achieved above the liquid where the emerged particles emit fluorescence induced by the laser. Toward the lower region, the liquid surface is distorted because of capillarity among the emerged

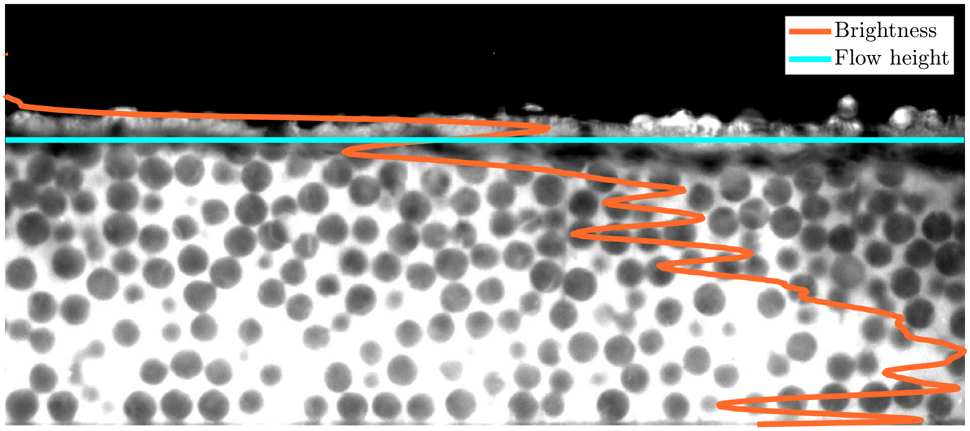

Fig. 3 Flow height determination. The averaged brightness profile and the flow height overlapped on an enhanced experimental image. The averaged brightness profile scales linearly with its distance from the image's left edge

particles, resulting in the reflection of the fluorescence and brightness here is reduced. The brightness increases again away from the surface. This picture gives the brightness a peak and a valley near the surface. In practice, the flow height H is set at the middle of the peak and valley. This procedure was found to be relatively stable and tracks well the height variation over the entire observation period.

Figure 4 provides the flow height variations over the observing duration for the experiments listed in Table 1. Note that the moment the granular flow arrives the triaxial piezoelectric is set as the zero time, which is determined by the abrupt rise of the signal. The variations of the experiments generally follow the same trend. After the passage of the flow front, H reaches a 4–5 s plateau (stage 1) followed by a 3–4 s rapid declination (stage 2), after which another 1–2 s plateau (stage 3) appears. The flow height is generally less than $10d \approx 38$ mm. So the flow height-width ratio is less than $38/200 = 0.19$ and can be seen as two-dimensional. The flow height declining rate is introduced and calculated as $\dot{H} = \Delta H / H_0 \Delta t$, where ΔH is the height decrease over period Δt, and H_0 is the initial height. It can be seen in Table 1 that $\dot{H}$ is generally less than 2.5% per second except in stage 2. Note that we average the results over 0.1 s, implying a height variation less than 0.25%, which is acceptable for the steady assumption. The height decrease results from the decrease of the granular flow discharge when the packing height and the bottom pressure in the silo decrease. Another indicator to quantify this unsteady effect is by

$$Q = \frac{\partial(HU)/\partial t}{gH\sin\theta} \sim \frac{H_0U_0 - H_1U_1}{gH\sin\theta\Delta t}, \tag{6}$$

where U is the depth-averaged velocity $U = \int_0^H u \mathrm{d}\xi / H$ (Bonnoit et al. 2010). Q can be seen as the flow acceleration (or deceleration) over the system's streamwise driving force $g\sin\theta$. Again, this quantity given in Table 1 is much smaller than unity, indicating that the flow can be considered a quasi-steady state.

For slope angle $\theta = 10.48°$, two laser entrance positions $\Delta y/W$ are used: 0.3 and 0.4. The two flow height variations shown in Fig. 4 are roughly the same, but the latter is delayed by about 1.0 s, as evidenced in the inset where a time shift is applied and good agreement is achieved. Note that for $\Delta y/W = 0.3$, the prepared material volume is 0.01 m^3 less than that for $\Delta y/W = 0.4$. This portion should be discharged first so that the flow properties can be comparable and the time needed corresponds to the time shift. The good agreement obtained by applying the time shift implies that there is no significant difference between the two slices and also the flow is history-independent.

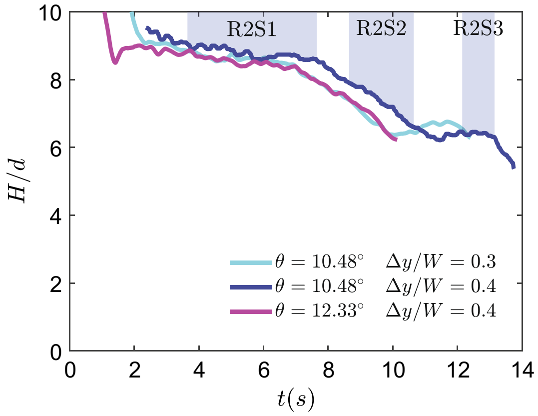

Fig. 4 Flow height variation. The shaded areas represent the analysed experimental periods for $\theta = 10.48°$, $\Delta y/W = 0.4$. Inset: the same, but the data for $\theta =°$ 10.48, $\Delta y/W = 0.4$ shifted forward by 1.0 s

4.2 Internal flow structure

Figure 5 gives the velocity distribution of the internal particles during R2S1 where only about 10% data is shown. The normal velocity w is generally close to zero, and the streamwise velocity u is the main component which increases with height and tends to a constant value for upper layers, similar to a plug flow. It can be seen that the particles are fully mobilised, and no sediment layer exists. Though the bottom plate is roughened, the near-bottom particles still slip remarkably which corresponds to a solid bed flow (Armanini et al. 2005). Note that the lowest layer actually moves in the gap where no particles are glued. However, the gap's influence on the upper flow is believed to be limited. Though w is significantly smaller than u, their fluctuations are comparable, as seen in Fig. 5 where both have significant scatter and

Table 1 Parameters of the experiments and the periods used for the analysis. Δt is the duration of the analysed period

$\theta(°)$	$\Delta y/W$	V_0 (m^3)	Period (s)	Δt (s)	$\dot{H}$ (1/s) (%)	Q	$\bar{\phi}$	Label	Marker
10.48	0.3	0.15	2.30–4.30	2	2.39	0.0286	0.4827	R1S1	○
10.48	0.4	0.16	3.65–7.65	4	1.36	0.0245	0.4805	R2S1	○
			8.65–10.65	2	8.20	0.1196	0.4655	R2S2	□
			12.15–13.15	1	2.41	0.0485	0.5028	R2S3	△
12.33	0.4	0.16	2.13–6.13	4	1.37	0.0260	0.4375	R3S1	○
			7.13–9.13	2	6.92	0.0725	0.4159	R3S2	□

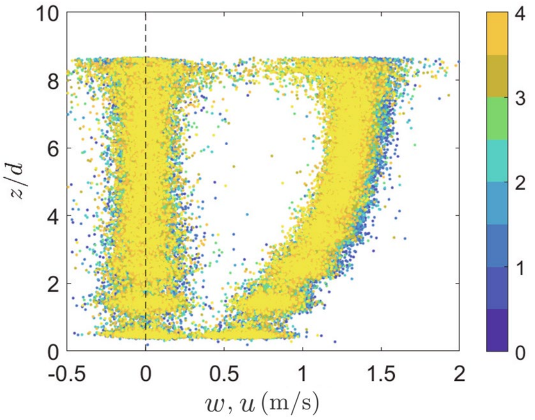

Fig. 5 The distribution of the velocity components for R2S1 (left cluster: normal velocity w; right cluster: streamwise velocity u)

comparable spans. The obviously increased velocity scattering at the upmost layer is actually due to poor particle detection and matching near the surface. The velocity component u decreases with time manifested as the brighter points turn to smaller values. However, w does not show such a trend and is essentially constant over time. The layer averaged velocity profiles shown in Fig. 6a confirm these trends and u decreases by about 10% during R2S1 which lasts 4 s.

The shear rate $\dot{\gamma}$ obtained by a central difference of the averaged velocity profile is given in Fig. 6b. It is shown that the shear occurs mainly near the bottom and the shear rate decreases monotonically with the flow height z. The granular temperature profile is shown in Fig. 6c. Similar to the shear rate, the granular temperature T decreases with increasing height, indicating that the near-bottom particles considerably collide with each other and fluctuate. The solid volume fraction ϕ shown in Fig. 6d increases with height in contrast to $\dot{\gamma}$ and T, implying that the granular flow is dilute ($\phi \approx 0.4$) near the bottom where significant shear and granular fluctuations occur, and that the flow is dense near the surface ($\phi \approx 0.55$) where the particles moves as a cluster and the shear is weak. Figure 6 shows that the velocity, shear rate and granular temperature distributions for different statistical intervals are similar during stage R2S1 but tend to decrease,

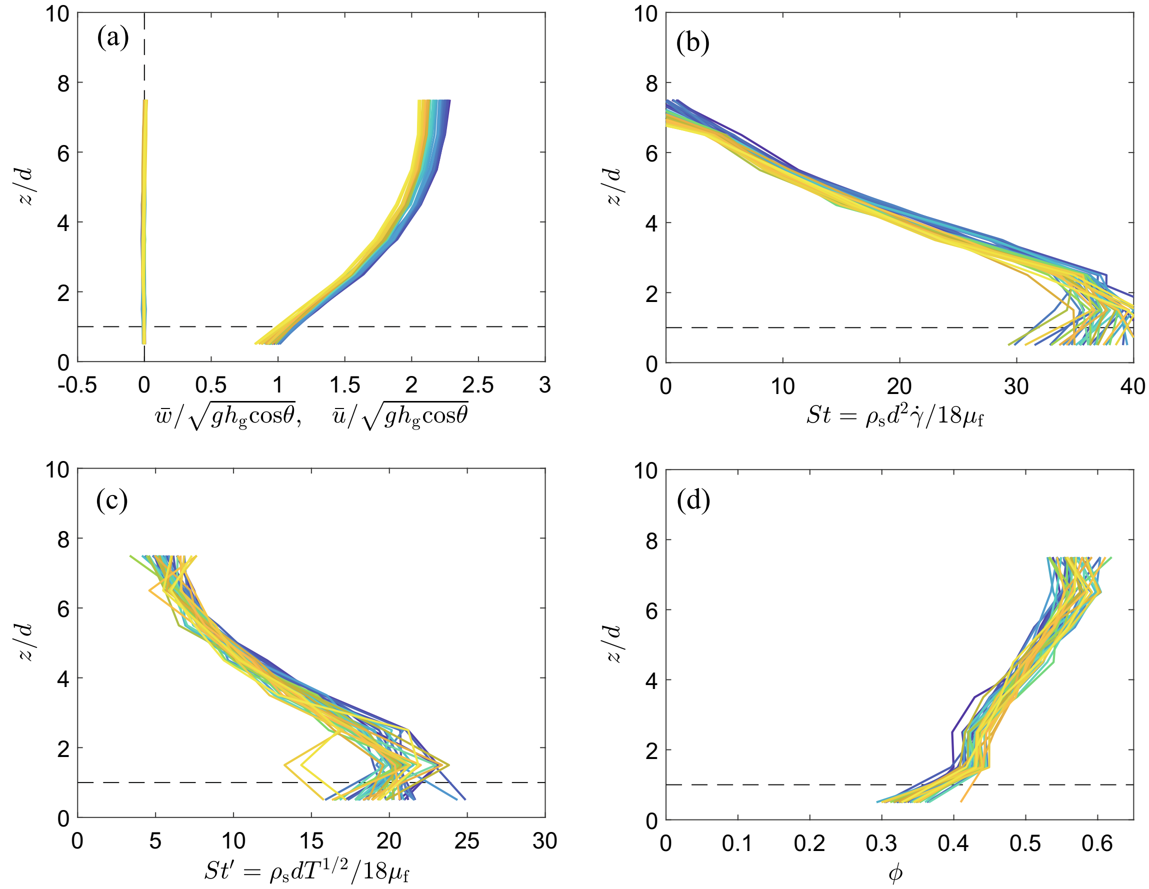

Fig. 6 Internal flow structures for R2S1. Layer-averaged **a** velocity, **b** shear rate, **c** granular temperature profiles and **d** solid volume fraction obtained from statistics on 0.1 s intervals over the duration of R2S1. The lines are coloured by their appearance time, with brighter being later, as indicated by the colour bar in Fig. 5. The lateral dashed line is at the height d below which the flow is in the gap

while the solid volume fraction tend to increase. Their correlation will be analysed in Sect. 5.2.

A comparison between cases is given in Fig. 7. Averaged results are provided approximately 2.5 s before the height decreasing stage (i.e. 5.15−5.25 s for R2S1 and 4.15−4.25 s for R1S1 and R3S1). Results at the mid-time of R2S2, R2S3 and R3S2 are also given. Comparing R2S1 and R3S1, Fig. 7a shows that an increasing slope angle results in a higher velocity in a way like that the velocity is shifted overall, and the shear rate is generally the same as shown in Fig. 7b. Concerning the profiles of the second run (R2, coloured blue), the velocity, shear rate and granular temperature constantly decrease when the flow is less mobile, while the packing density increases, which is also evidenced by the depth-averaged volume fraction $\bar{\phi}$ given in Table 1. Concerning R1S1, the observation plane is closer to the sidewall, and the velocity is slightly reduced compared with R2S1 for less than 2%, as shown in Fig. 7a. The two have very close profiles of flow structures, indicating that the wall influence at the inner observing position $\Delta y/W = 0.4$ is already small. Though the flow three-dimensionality may be significant near the side wall, the flows observed at the internal position are nearly two-dimensional.

4.3 Performance of the dynamic properties measurement

A representative picture of the recorded signal is shown in Fig. 8, where the sensors' output signals are converted to physical values and normalised. The arrival of the flow front, which is about two times higher than the gate opening, generates dynamic peaks in the bottom pressure and stresses. This steep flow front is characteristic of a typical debris flow (Iverson 1997; Berzi et al. 2010). After the front, the flow height rapidly decreases and becomes a nearly uniform, quasi-steady flow, also called body in debris flow. This stage is of primary interest in this study, where the images of internal flow are captured and analysed.

Note that the pressures and stresses in Fig. 8 are properly normalised by the corresponding gravity component and density so that they have a flow height meaning. For the stresses, the mixture density is used assuming $\phi = 0.5$. It is shown that the variation of the directly measured pressures

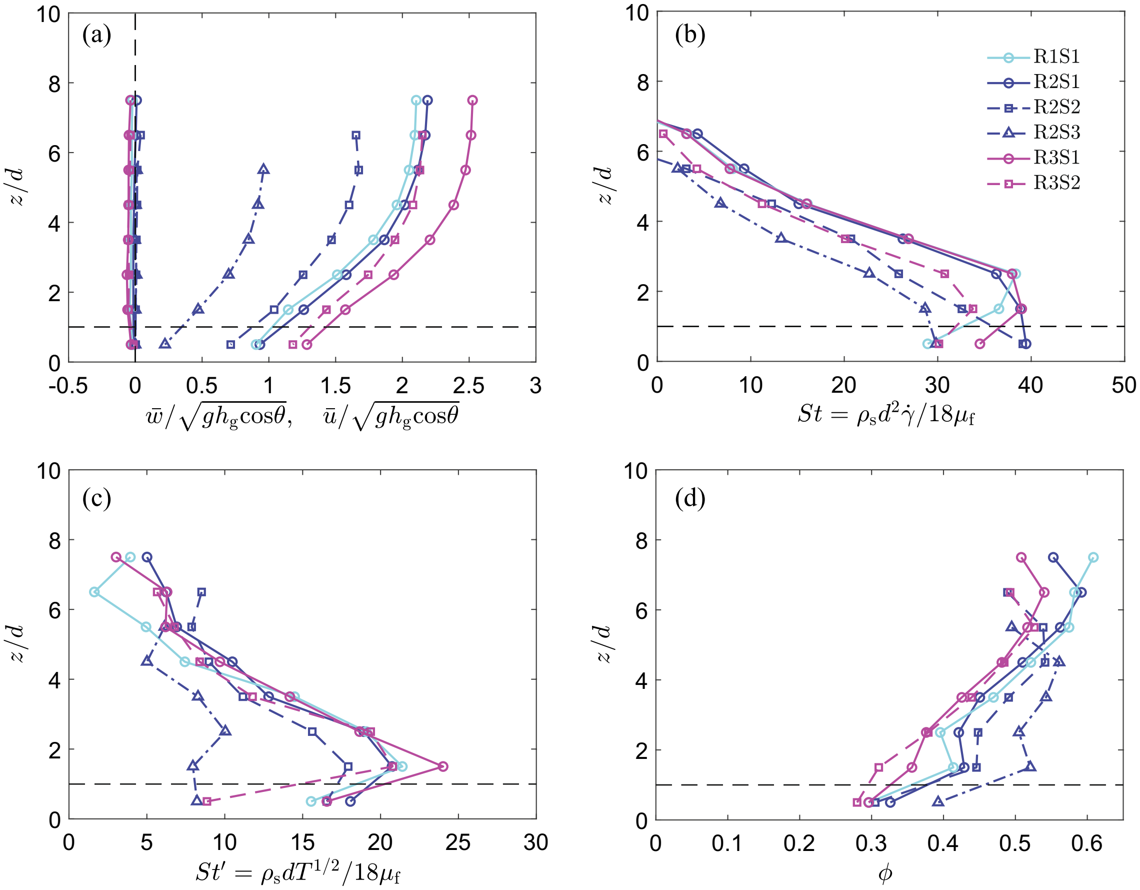

Fig. 7 Representative internal flow structures for **a** averaged velocity components, **b** shear rate, **c** granular temperature, and **d** solid volume fraction

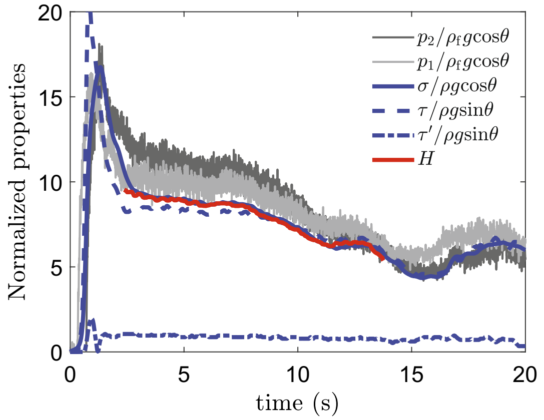

Fig. 8 Representative example of the normalised measured bottom stresses and pressures for $\theta = 10.48°$, $\Delta y/W = 0.4$. The flow height obtained from image processing is also shown. The vertical axis is normalised by the particle diameter d

and stresses match the flow height well. The overlap of the normalised normal stress with the flow height indicates that the gravity-balanced expression given by Eq. (4) is reasonable. However, the shear stress presents a slight deviation (5–10%) from H, which is likely due to the tangential force measurement uncertainty. The transverse shear stress τ' remains quite small and stable, indicating that no apparent transverse flow or asymmetry exists.

The close matching of the normalised pressure p_1 to the flow height implies that the bottom pore pressure is close to the hydrostatic pressure given by $p_1 = \rho_{\mathrm{f}} g H \cos\theta$. Note that p_1 corresponds to the upstream measuring point and is closer to the observing area. The hydrostatic pressure is actually predictable because the Darcy number, defined as $Da = \mu_{\mathrm{f}}/\phi\rho_{\mathrm{s}}k\dot{\gamma}$ (permeability k), is evaluated to be 1.77, which is small enough that the granular media exhibit large conductivity and negligible excess pore pressure (Lanzoni et al. 2017).

Another aspect worth investigating is the performance of Eqs. (3) and (4) in calculating the bottom stresses τ_{c} and σ_{c} compared with the sensor-measured values τ_{m} and σ_{m}. Figure 9 shows that the calculated stresses match the measured stresses well, with the deviation generally less than 10%. However, the shear stress presents larger deviations, as also evidenced in Fig. 8. Note that the edges of the 100 mm squared load plate lie in $\Delta y/W = 0.25$, where the shear stresses from side mixtures may play a role and result in a smaller measured bottom shear stress. Besides, the measured shear stress bias is as much as 10% itself, as described in Sect. 2.2. So the normal stresses are believed to be more reliable and to provide a more meaningful comparison. Equations (3) and (4) are seen as providing good estimations of the stresses.

5 Discussions

5.1 Kinetic theory in predicting stresses

The internal flow information including velocity u, w, shear rate $\dot{\gamma}$, granular temperature T, packing density ϕ and interparticle stresses τ, σ' at each elevations and flow stages is now obtained. This section examines their correlations by the widely used kinetic theory of granular flow which relates the granular stresses to the flow state (T, $\dot{\gamma}$, ϕ) and the material properties (Jenkins and Savage 1983; Jenkins 2007; Berzi and Fraccarollo 2015). The equation of state for granular pressure reads

$$\frac{\sigma'}{\rho_{\mathrm{s}}T} = \phi\left[1 + 4\phi g_0(\phi)\frac{1+e_{\mathrm{f}}}{2}\right]\left[1 + \frac{\rho_{\mathrm{f}}}{\rho_{\mathrm{s}}}a(\phi)\right] \tag{7}$$

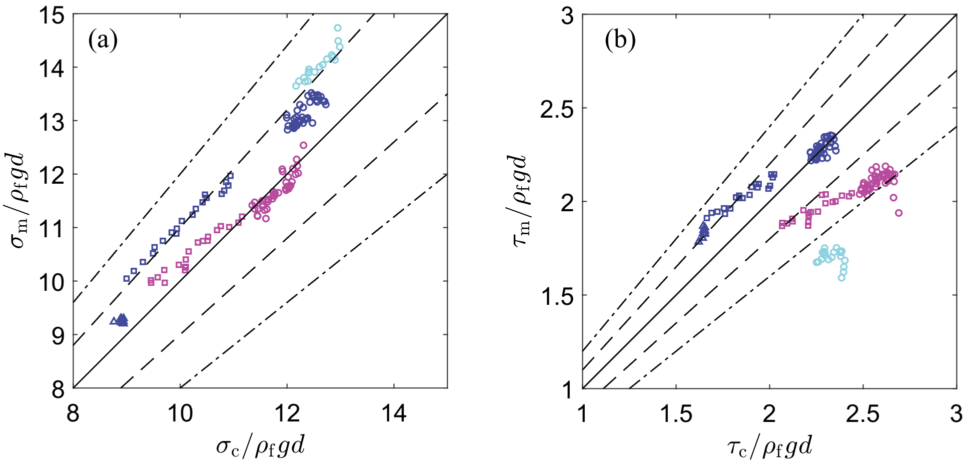

Fig. 9 Comparison of the calculated (lateral axis) and measured (vertical axis) **a** normal stresses and **b** shear stresses. Marker representations are provided in Table 1. The dashed and dash-dotted lines represent ±10% and ±20% deviations, respectively

where $g_0(\phi)$ is the radial distribution function and the expression given by Vescovi et al. (2014) is adopted:

$$g_0(\phi) = \frac{2-\phi}{2(1-\phi)^3} \tag{8}$$

i.e. Carnahan–Starling's expression for $\phi \le 0.4$ and

$$\begin{aligned} g_0(\phi) = {} & \left[1 - \left(\frac{\phi - 0.4}{\phi_c - 0.4}\right)^2\right] \frac{2-\phi}{2(1-\phi)^3} \\ & + \left(\frac{\phi - 0.4}{\phi_c - 0.4}\right)^2 \frac{2}{\phi_c - \phi} \end{aligned} \tag{9}$$

for $\phi > 0.4$ which ensures a divergence at random close packing density $\phi_c = 0.64$. e_f is the effective coefficient of restitution which implicitly considers the loss of transitional kinetic energy due to particle rotation (Gollin et al. 2017), and is related to particle coefficient of restitution e and friction coefficient μ_s as (Chialvo and Sundaresan 2013)

$$e_f = e - \frac{3}{2}\mu_s \exp(-3\mu_s) \tag{10}$$

which results in $e_f \approx 0.74$ for the glass particles used in the experiments.

The second factor with bracket at the right hand of Eq. (7) represents the contribution of the added mass effect to the granular pressure in liquid-particle mixture flows considering the fact that the particles' acceleration or deceleration will induce conjugate motion of the surrounding liquid. As introduced by Armanini et al. (2005), $a(\phi) = (1 + 2\phi)/(2(1 - \phi))$ which reduce to 1/2 in dilute regime when $\phi \to 0$ and presents more contribution with increasing packing density.

The corresponding shear stress is given by

$$\frac{\tau}{\rho_s d\dot{\gamma}\sqrt{T}} = \frac{8J\phi^2 g_0}{5\sqrt{\pi}}\left(1 + \frac{\rho_f}{\rho_s} a(\phi)\right) \tag{11}$$

where the coefficient J is

$$J = \frac{1+e_f}{2} + \frac{\pi}{32}\frac{\left[5 + 2(1+e_f)(3e_f - 1)g_0\right]\left[5 + 4(1+e_f)g_0\right]}{\left[24 - 6(1-e_f)^2 - 5(1-e_f^2)\right]g_0^2}. \tag{12}$$

The comparisons of the experimental results and the prediction of the kinetic theory are given in Fig. 10. It can be seen that the experimental results follows well the trend given by Eqs. (7) and (11). The inclusion of the added mass effect clearly improves the kinetic theory prediction in liquid-particle mixture flows by comparing the solid (with) and dashed (without) curves. The increasing data scattering at higher packing density is due to that the granular temperature is decreasing to near zero and the extrapolation of the ACF leads to more uncertainty. It is observed that the prediction by the kinetic theory is generally smaller than the experimental data and the curves provide a lower bound to the pressure or shear stress. It is well known that the kinetic theory is appreciated in the dilute regime where binary collisions dominates the particles contact which may not be satisfactorily met in the experiments and results in the lower prediction. Besides, the modification considering the added mass effect, though significantly improves the prediction, is still an idealised version and some other important features may be missed (Armanini et al. 2005). Despite the above issues, Fig. 10 shows that the internal flow information reported in this paper reasonably agrees with the present knowledge on the granular flow and kinetic theory.

5.2 Particle interaction patterns

Dense granular flows are dominated by inter-particle interactions such as frictions and collisions which exhibit different rheological characteristics under different particle interaction patterns (Armanini et al. 2005). For example, in the inertial flow regime where particles are seen as collision-dominated, Bagnold (1954) found that the stresses scale quadratically with shear rate as $\tau \propto \rho_s d^2\dot{\gamma}^2$. This section focuses on the rheological characteristics and the particle interaction patterns.

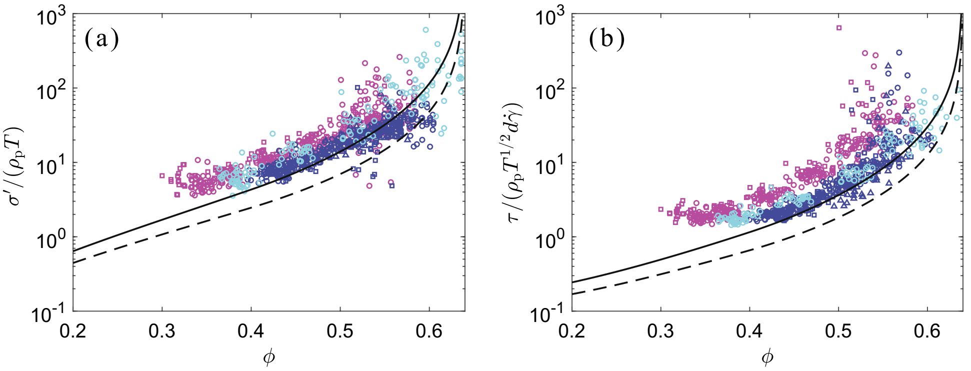

Fig. 10 Dimensionless **a** effective normal stress and **b** shear stress compared with the prediction of kinetic theory. The solid lines in **a** and **b** represents Eqs. (7) and (11) respectively and the dashed lines are the corresponding predictions without added mass effect

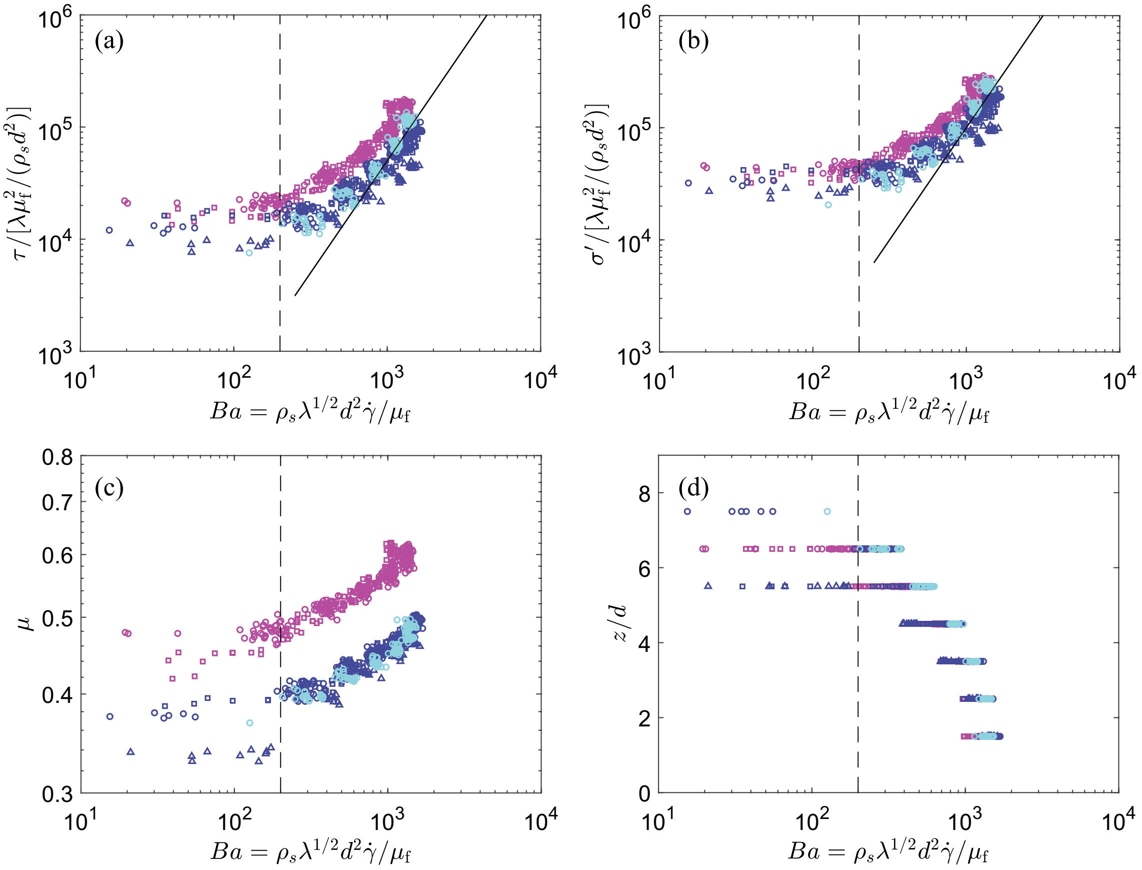

Fig. 11 Relationship of the **a** shear stress, **b** effective normal stress, and **c** friction coefficient to the shear rate (Bagnold number, *Ba*). **d** Distribution of *Ba* along the flow depth. The solid lines in **a** and **b** represent the Bagnoldian rheology as $\tau, \sigma' \propto \rho_s d^2\dot{\gamma}^2$. The dashed lines correspond to $Ba = 200$

Figure 11a, b shows the relationship between stresses and shear rate. Here, the normalised stresses $\tau/[\lambda\mu_f^2/(\rho_s d^2)]$ and $\sigma'/[\lambda\mu_f^2/(\rho_s d^2)]$ and shear rate $Ba = \rho_s\lambda^{1/2}d^2\dot{\gamma}/\mu_f$ (Bagnold number) are introduced following Armanini et al. (2005), where $\lambda = 1/[(\phi_0/\phi)^{1/3} - 1]$ and $\phi_0 = 0.74$. The stresses follow the Bagnoldian rheology at high shear rates (large *Ba*), implying a collision-dominated inertial regime. At low *Ba*, however, the stresses become rate-independent, and the fiction coefficient $\mu = \tau/\sigma'$ given in Fig. 10c tends to be constant, implying a frictional regime. This friction—collision description is in accordance with Armanini et al. (2005), even though different flow conditions are applied. The transition occurs at roughly $Ba^* \approx 200$, which corresponds to the position approximately $z > 6d$, as shown in Fig. 10d. Therefore, the particle interaction pattern is stratified with a collision-dominated near-bottom flow and a friction-dominated upper flow. Note that the transition point may be influenced by the fluid viscosity, as argued by Armanini et al. (2005) and is reported to be $Ba^* \approx 1000$ in their work. A deeper investigation of this issue may be required but is beyond the scope of this study.

5.3 Coherence length

It has been pointed out that the dominating particle interaction pattern is stratified, and different stress-generating mechanisms exist. The particle interaction pattern is now further examined based on the coherence length approach. Similar to the pioneering Prandtl mixing length for turbulent Reynolds stress modelling, a coherence length scale l is introduced, and the shear stress is written as

$$\tau = \rho l^2 \dot{\gamma}^2. \tag{13}$$

The coherence length l can be seen as the characteristic size of the granular clusters in the flow (MiDi 2004) and is related to the particle interaction length scale in different stress-generating mechanisms (Lanzoni et al. 2017). Figure 12 provides the distribution of l deduced from Eq. (13) as $l = \sqrt{\rho l^2 \dot{\gamma}^2}$. It is seen that near the bottom, l is of the order of $1 - 2d$ indicating a Bagnoldian rheology or collision-dominated behaviour, as also demonstrated in Sect. 5.2. Turning to the upper layer, the coherence length gradually

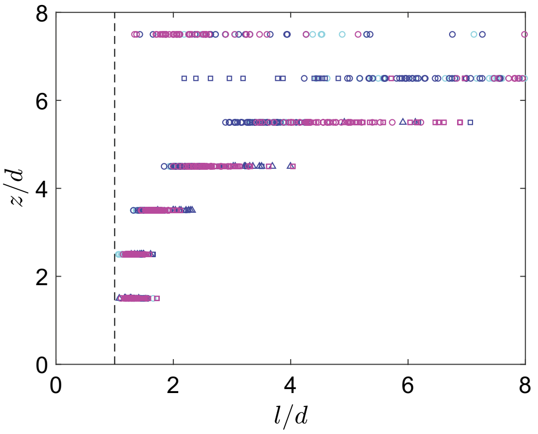

Fig. 12 Distribution of the coherence length

increases to about $6-8d$ near the flow surface, where the particle interaction is friction-dominated.

The coherence length approach combined with the internal flow structure provides a more physical and comprehensive interpretation of the particle interaction pattern. The bottom plate has a glued layer of particles which cause significant collisions with the flowing particles. The coherence length here is the typical travelling distance for a collision to occur, i.e. $1-2d$. These collisions generate significant particle fluctuations, and the particles are *heated* and possess high granular temperatures. These bottom particles collide with the upper layer and transmit the fluctuation energy upward. However, the fluctuation energy is gradually damped by the inter-particle inelastic interactions and liquid-particle interaction (lubrication and drag force). Therefore, the granular temperature decreases with increasing distance from the bottom, as shown in Fig. 6c. The fluctuations are generally exhausted near the surface, where the particles interact through long-lasting contact dominated by the friction behaviour. Here, the particles transfer momentum through force networks and the resulting coherence length increases to several diameters.

6 Conclusions

The quasi-steady liquid-particle mixture flow down an inclined channel is studied experimentally using the refractive index matching method, which gives the internal flow structures including the velocity, solid concentration, shear rate and granular temperature. The pore pressure and stress under the flow are measured and analysed combined with the internal kinetic flow properties. The bottom pressure follows the hydrostatic pressure distribution given the adopted large conductivity flow condition. The measured bottom stresses agree well with those calculated by the gravity balance assumption, which confirms the reliability of the stress calculation method adopted.

The flow develops in three stages after the passage of the flow front: plateau, rapid decrease, and another short duration plateau. The plateau flow is found to be in a quasi-steady state, manifesting as small flow property (height and velocity) variations over the statistical intervals. The internal flow information presented is examined to be almost immune from the wall influence when $\Delta y/W$ approaches 0.4, indicating that the reported flow properties is almost undisturbed by the sidewall and more representative of a true granular flow. The internal flow properties agree well the prediction of the kinetic theory considering the added mass effect. The flow is found to be rheologically stratified from the relationship between stress and shear rate. The near-bottom region is collision-dominated, where large deformations exist, and the stress follows the Bagnoldian rheology. The flowing particles near the bottom frequently collide with the bottom fixed particles, inducing high granular temperatures. The particle-particle interaction near the upper surface is friction-dominated, where the flow moves like a plug with no significant deformation and where the coherence length is several diameters, indicating that long-lasting contact exists.

This paper presents the first results of a longer-term study. Further work will be devoted to other flow conditions with varying inclinations or gate openings (flow rates) to study their internal flow properties and particle interaction patterns. The flow difference between observing positions is also a topic worthy of investigation and will be studied systematically in future research. Moreover, the particle concentration as a primary flow parameter deserves taken good care of to build its relationship with the area fraction or other information that can be characterised from the images, and a calibration procedure may be needed.

Appendix A: assumption of fully developed flow

Since the spatial development by measuring the results at different streamwise locations is unavailable for now, we have to assume that the flow is already fully developed at the observing position, i.e. the flow variation along the streamwise direction is negligible. However, two evidences can help support this assumption. Firstly, we have not observed obvious flow height variation spatially along the channel during the plateau stage. Secondly, the experimental setup conditions of the relevant investigations whose granular flows were formed by releasing the upstream mass, similar with the present study, are compared in Table 2. Though the detailed flow condition varies, such as the material properties, velocities, inclinations, here we simply compare the

Table 2 Comparison of the observing positon with previous investigations

Investigations	X (mm)	H (mm)	X/H	Flow condition
Bonnoit et al. (2010)	1000	5	200	Granular suspension
Aussillous et al. (2013)	500	65	7.69	Sediment transport
Lanzoni et al. (2017)	5400, 7800	50	108, 156	Water-particle flow
Pouliquen (1999)	200–500	2–12.5	16–250	Dry
Roche et al. (2021)	540, 980	10	54, 98	Dry
Present	2400	38	63.16	Liquid-particle flow

ratio of the observing distance X from the inlet to a characteristic flow height H. This paper sets the observing position at a distance X of 2.4 m away from the channel inlet. The flow height H is generally less than $10d \approx 38$ mm, leading to a distance-height ratio of $X/H = 2400/38 \approx 63$. It can be seen that the ratio adopted in the present study is within a reasonable range of the previous investigations. So the flow is believed to be fully developed at the observing position.

Appendix B: Granular temperature estimation

The granular temperature is defined as $T = (\overline{u'^2} + \overline{w'^2})/2$ where the velocity fluctuation is traditionally calculated in a mean-squared (MS) way. However, it is noticed that the MS-based fluctuation results in artifacts due to accumulation of measurement noise from the particle location identification and matching process (Armanini et al. 2005; Gollin et al. 2017; Taylor-Noonan et al. 2021). An alternative estimation is based on the Lagrangian velocity auto-correlation function (ACF) defined as $\langle u'(t)u'(t+\delta t)\rangle$ (Larcher et al. 2007). It is found theoretically that the function follows an exponential law with δt as $\langle u'(t)u'(t+\delta t)\rangle = \langle u'(t)u'(t)\rangle \exp(-|\delta t|/t_0)$ (Armanini et al. 2005). For each statistical period $t_s = 0.1$ s, the particles are tracked for at least ten frames (0.01 s) forward and backward. A typical result of the ACF is given in Fig. 13a. It is found that the ACF generally follows the exponential law and convergences to zero with increasing δt. In practice, only the first 2–10 data points are used for the exponential fit and then extrapolated back to $\delta t = 0$ giving the fluctuation $(\overline{u'^2})_{\mathrm{ACF}}$. It is seen that the fluctuation based on ACF is generally smaller than the MS-based, i.e. the cross at $\delta t = 0$ in Fig. 13a. The normal fluctuation $\overline{w'^2}$ is obtained in the same way which has comparable magnitude with $\overline{u'^2}$. Two estimations of the granular temperature T_{ACF} and T_{MS} are obtained as given in Fig. 13b. It is obvious that T_{ACF} which is believed to be less affected by the measurement noise is smaller than T_{MS}. For the upmost statistical bin, the

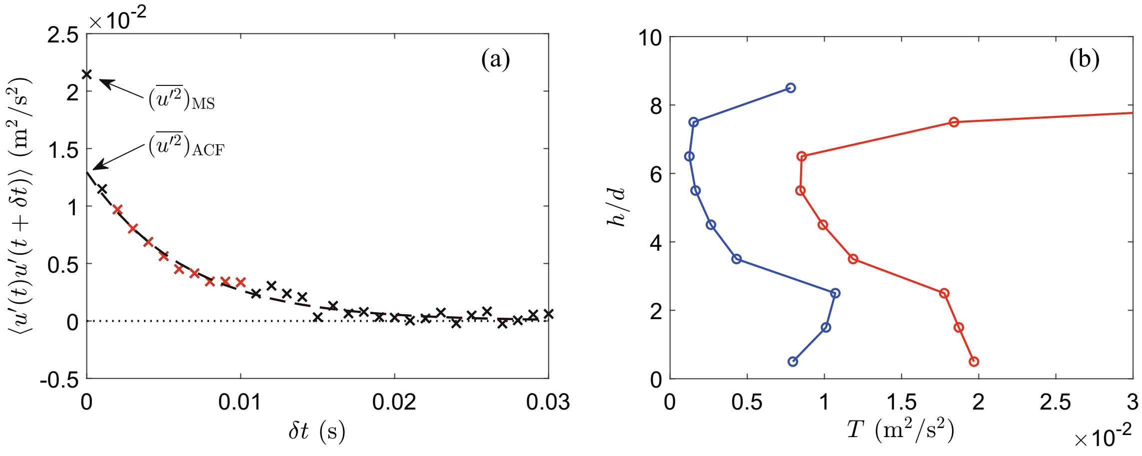

Fig. 13 **a** Lagrangian velocity auto-correlation function. The dashed line is the exponential fit of the red crosses. **b** Comparison of T_{ACF} (blue) and T_{MS} (red)

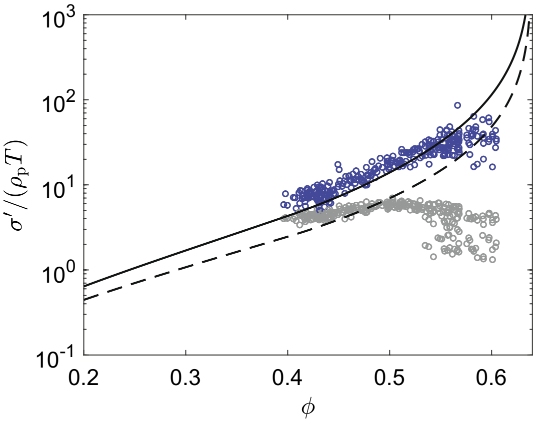

Fig. 14 Dimensionless effective normal stress compared with the prediction of kinetic theory for R2S1. The blue and grey markers are the results based on T_{ACF} and T_{MS} respectively

increase of granular temperature is actually due to poor particle tracking performance near the flow surface. Though T_{MS} have similar trend with T_{ACF} along the flow height, it performs badly in predicting the stresses when applied to kinetic theory (see Sect. 5.1). As shown in Fig. 14, T_{MS} leads to significantly small results compared with kinetic theory and even wrong direction opposite to the theoretical curves with increasing packing density. So the ACF-based granular temperature T_{ACF} is more credible and is adopted in this study.

Supplementary Information The online version contains supplementary material available at https://doi.org/10.1007/s00348-023-03691-y.

Acknowledgements We thank LiBin Li and Can Huang for their helpful assistance in performing part of the experiments. We also thank Robert A. Brewster, PhD for editing the English text of a draft of this manuscript.

Author contributions Conceptualization: QL, YA; methodology: YA, YS; Formal experiment and analysis: YS, JJ; writing: YS, XW, QL; funding acquisition and supervision: XW, QL.

Funding The work was supported by the National Natural Sciences Foundation of China (Grant No. 12032005, 12172057).

Data availability The data that support the findings of this study are available from the corresponding authors upon reasonable request.

Declarations

Conflict of interest The authors report no conflict of interest.

Ethical Approval Not applicable

References

Andreotti B, Forterre Y, Pouliquen O (2013) Granular media: between fluid and solid. Cambridge University Press, Cambridge

Armanini A, Capart H, Fraccarollo L, Larcher M (2005) Rheological stratification in experimental free-surface flows of granular-liquid mixtures. J Fluid Mech 532:269–319. https://doi.org/10.1017/s0022112005004283

Armanini A, Larcher M, Fraccarollo L (2009) Intermittency of rheological regimes in uniform liquid-granular flows. Phys Rev E 79(5):051306. https://doi.org/10.1103/PhysRevE.79.051306

Atherton TJ, Kerbyson DJ (1999) Size invariant circle detection. Image Vis Comput 17(11):795–803. https://doi.org/10.1016/S0262-8856(98)00160-7

Aussillous P, Chauchat J, Pailha M, Médale M, Guazzelli É (2013) Investigation of the mobile granular layer in bedload transport by laminar shearing flows. J Fluid Mech 736:594–615. https://doi.org/10.1017/jfm.2013.546

Bagnold R (1954) Experiments on gravity-free dispersion of large solid spheres in a Newtonian fluid under shear. Proc R Soc A Math Phys Eng Sci 225:49–63. https://doi.org/10.1098/rspa.1954.0186

Berzi D, Fraccarollo L (2015) Turbulence locality and Granularlike fluid shear viscosity in collisional suspensions. Phys Rev Lett 115(19):194501

Berzi D, Jenkins JT, Larcher M (2010) Debris flows: recent advances in experiments and modeling. Adv Geophys 52:103–138

Bonnoit C, Darnige T, Clement E, Lindner A (2010) Inclined plane rheometry of a dense granular suspension. J Rheol 54(1):65–79. https://doi.org/10.1122/1.3258076

Brodu N, Delannay R, Valance A, Richard P (2015) New patterns in high-speed granular flows. J Fluid Mech 769:218–228. https://doi.org/10.1017/jfm.2015.109

Capart H, Fraccarollo L (2011) Transport layer structure in intense bed-load. Geophys Res Lett 38(20):L20402. https://doi.org/10.1029/2011gl049408

Capart H, Young D, Zech Y (2002) Voronoï imaging methods for the measurement of granular flows. Exp Fluids 32(1):121–135

Cassar C, Nicolas M, Pouliquen O (2005) Submarine granular flows down inclined planes. Phys Fluids 17(10):103301

Chauchat J (2018) A comprehensive two-phase flow model for unidirectional sheet-flows. J Hydraul Res 56(1):15–28

Chialvo S, Sundaresan S (2013) A modified kinetic theory for frictional granular flows in dense and dilute regimes. Phys Fluids 25(7):070603

Dijksman JA, Rietz F, Lorincz KA, van Hecke M, Losert W (2012) Invited article: Refractive index matched scanning of dense granular materials. Rev Sci Instrum 83(1):011301. https://doi.org/10.1063/1.3674173

Ferdowsi B, Ortiz CP, Houssais M, Jerolmack DJ (2017) River-bed armouring as a granular segregation phenomenon. Nat Commun 8(1):1363. https://doi.org/10.1038/s41467-017-01681-3

Forterre Y, Pouliquen O (2001) Longitudinal vortices in granular flows. Phys Rev Lett 86(26 Pt 1):5886–9. https://doi.org/10.1103/PhysRevLett.86.5886

Forterre Y, Pouliquen O (2008) Flows of dense granular media. Annu Rev Fluid Mech 40(1):1–24. https://doi.org/10.1146/annurev.fluid.40.111406.102142

Gollin D, Brevis W, Bowman ET, Shepley P (2017) Performance of piv and ptv for granular flow measurements. Granular Matter 19(3):42

Guazzelli É, Pouliquen O (2018) Rheology of dense granular suspensions. J Fluid Mech 852:P1. https://doi.org/10.1017/jfm.2018.548

Hanes DM, Walton OR (2000) Simulations and physical measurements of glass spheres flowing down a bumpy incline. Powder Technol 109(1):133–144. https://doi.org/10.1016/S0032-5910(99)00232-6

Houssais M, Ortiz CP, Durian DJ, Jerolmack DJ (2015) Onset of sediment transport is a continuous transition driven by fluid shear and granular creep. Nat Commun 6:6527. https://doi.org/10.1038/ncomms7527

Houssais M, Ortiz CP, Durian DJ, Jerolmack DJ (2016) Rheology of sediment transported by a laminar flow. Phys Rev E 94(6–1):062609. https://doi.org/10.1103/PhysRevE.94.062609

Iverson RM (1997) The physics of debris flows. Rev Geophys 35(3):245–296. https://doi.org/10.1029/97rg00426

Iverson RM, George DL (2019) Basal stress equations for granular debris masses on smooth or discretized slopes. J Geophys Res Earth Surf 124(6):1464–1484. https://doi.org/10.1029/2018jf004802

Iverson RM, Logan M, LaHusen RG, Berti M (2010) The perfect debris flow? aggregated results from 28 large-scale experiments. J Geophys Res 115(F3):F03005. https://doi.org/10.1029/2009jf001514

Jenkins JT (2007) Dense inclined flows of inelastic spheres. Granular Matter 10(1):47–52. https://doi.org/10.1007/s10035-007-0057-z

Jenkins JT, Savage SB (1983) A theory for the rapid flow of identical, smooth, nearly elastic, spherical particles. J Fluid Mech 130:187–202. https://doi.org/10.1017/S0022112083001044

Jop P, Forterre Y, Pouliquen O (2005) Crucial role of sidewalls in granular surface flows: consequences for the rheology. J Fluid Mech 541(1):167. https://doi.org/10.1017/s0022112005005987

Jop P, Forterre Y, Pouliquen O (2006) A constitutive law for dense granular flows. Nature 441(7094):727–30. https://doi.org/10.1038/nature04801

Lanzoni S (1993) Meccanica di miscugli solido-liquido in regime granulo-inerziale. Thesis

Lanzoni S, Gregoretti C, Stancanelli LM (2017) Coarse-grained debris flow dynamics on erodible beds. J Geophys Res Earth Surf 122(3):592–614. https://doi.org/10.1002/2016jf004046

Larcher M, Fraccarollo L, Armanini A, Capart H (2007) Set of measurement data from flume experiments on steady uniform debris flows. J Hydraul Res 45(sup1):59–71. https://doi.org/10.1080/00221686.2007.9521833

Matoušek V, Zrostlík Š, Fraccarollo L, Prati A, Larcher M (2019) Internal structure of intense collisional bedload transport. Earth Surf Proc Land 44(11):2285–2296

Maurin R, Chauchat J, Frey P (2016) Dense granular flow rheology in turbulent bedload transport. J Fluid Mech 804:490–512. https://doi.org/10.1017/jfm.2016.520

Maurin R, Chauchat J, Frey P (2018) Revisiting slope influence in turbulent bedload transport: consequences for vertical flow structure and transport rate scaling. J Fluid Mech 839:135–156. https://doi.org/10.1017/jfm.2017.903

Meninno S, Armanini A, Larcher M (2018) Gravity-driven, dry granular flows over a loose bed in stationary and homogeneous conditions. Phys Rev Fluids 3(2):024301. https://doi.org/10.1103/PhysRevFluids.3.024301

MiDi GDR (2004) On dense granular flows. Eur Phys J E Soft Matter 14(4):341–65. https://doi.org/10.1140/epje/i2003-10153-0

Ni W, Capart H (2018) Stresses and drag in turbulent bed load from refractive index-matched experiments. Geophys Res Lett 45(14):7000–7009

Ni WJ, Capart H (2015) Cross-sectional imaging of refractive-index-matched liquid-granular flows. Exp Fluids 56(8):163. https://doi.org/10.1007/s00348-015-2034-3

Perng ATH, Capart H, Chou HT (2005) Granular configurations, motions, and correlations in slow uniform flows driven by an inclined conveyor belt. Granular Matter 8(1):5–17. https://doi.org/10.1007/s10035-005-0213-2

Pouliquen O (1999) Scaling laws in granular flows down rough inclined planes. Phys Fluids 11(3):542–548. https://doi.org/10.1063/1.869928

Roche O, van den Wildenberg S, Valance A, Delannay R, Mangeney A, Corna L, Latchimy T (2021) Experimental assessment of the effective friction at the base of granular chute flows on a smooth incline. Phys Rev E 103(4–1):042905. https://doi.org/10.1103/PhysRevE.103.042905

Rousseau G, Ancey C (2020) Scanning piv of turbulent flows over and through rough porous beds using refractive index matching. Exp Fluids 61(8):172. https://doi.org/10.1007/s00348-020-02990-y

Sanvitale N, Bowman ET (2012) Internal imaging of saturated granular free-surface flows. Int J Phys Model Geotech 12(4):129–142. https://doi.org/10.1680/ijpmg.12.00002

Sanvitale N, Bowman ET (2016) Using piv to measure granular temperature in saturated unsteady polydisperse granular flows. Granul Matter 18(3):57. https://doi.org/10.1007/s10035-016-0620-6

Silbert LE, Ertas D, Grest GS, Halsey TC, Levine D, Plimpton SJ (2001) Granular flow down an inclined plane: Bagnold scaling and rheology. Phys Rev E 64(5):051302

Spinewine B, Capart H, Larcher M, Zech Y (2003) Three-dimensional voronoï imaging methods for the measurement of near-wall particulate flows. Exp Fluids 34(2):227. https://doi.org/10.1007/s00348-002-0550-4

Sun Y, Zhang W, An Y, Liu Q, Wang X (2021) Experimental investigation of immersed granular collapse in viscous and inertial regimes. Phys Fluids 33(10):103317. https://doi.org/10.1063/5.0067485

Sun Yh, Wt Zhang, Xl Wang, Qq Liu (2020) Numerical study on immersed granular collapse in viscous regime by particle-scale simulation. Phys Fluids 32(7):073313. https://doi.org/10.1063/5.0015110

Takahashi T (1978) Mechanical characteristics of debris flow. J Hydraul Div 104(8):1153–1169

Taylor-Noonan AM, Gollin D, Bowman ET, Take WA (2021) The influence of image analysis methodology on the calculation of granular temperature for granular flows. Granular Matter 23(4):96. https://doi.org/10.1007/s10035-021-01153-y

Trewhela T, Ancey C (2021) A conveyor belt experimental setup to study the internal dynamics of granular avalanches. Exp Fluids 62(10):207. https://doi.org/10.1007/s00348-021-03299-0

Underwood EE (1969) Stereology, or the quantitative evaluation of microstructures. J Microsc 89(2):161–180. https://doi.org/10.1111/j.1365-2818.1969.tb00663.x

Vescovi D, Berzi D, Richard P, Brodu N (2014) Plane shear flows of frictionless spheres: Kinetic theory and 3d soft-sphere discrete element method simulations. Phys Fluids 26(5):053305

Wiederseiner S, Andreini N, Epely-Chauvin G, Ancey C (2010) Refractive-index and density matching in concentrated particle suspensions: a review. Exp Fluids 50(5):1183–1206. https://doi.org/10.1007/s00348-010-0996-8

Wright SF, Zadrazil I, Markides CN (2017) A review of solid-fluid selection options for optical-based measurements in single-phase liquid, two-phase liquid-liquid and multiphase solid-liquid flows. Exp Fluids 58(9):108. https://doi.org/10.1007/s00348-017-2386-y

Yuen H, Princen J, Illingworth J, Kittler J (1990) Comparative study of hough transform methods for circle finding. Image Vis Comput 8(1):71–77

Zhang WT, An Y, Liu QQ, Wang XL, Sun YH (2020) Evolution of energy in submerged granular column collapse. Chin Phys Lett 37(7):074502. https://doi.org/10.1088/0256-307x/37/7/074502

Zhu Y, Delannay R, Valance A (2020) High-speed confined granular flows down smooth inclines: scaling and wall friction laws. Granul Matter 22(4):82. https://doi.org/10.1007/s10035-020-01053-7

Publisher's Note Springer Nature remains neutral with regard to jurisdictional claims in published maps and institutional affiliations.

Springer Nature or its licensor (e.g. a society or other partner) holds exclusive rights to this article under a publishing agreement with the author(s) or other rightsholder(s); author self-archiving of the accepted manuscript version of this article is solely governed by the terms of such publishing agreement and applicable law.